Fabrication, microstructure and mid-infrared luminescence of Er:$(Sc_xY_{1-x})_2O_3$ transparent ceramics

Roman Maksimov[a,b], Vladislav Shitov[a], Vladimir Osipov[a], Oleg Samatov[a], Dmitry Vakalov[c], Fedor Malyavin[c], Liza Basyrova[d], Pavel Loiko[d], and Patrice Camy[d,*]

[a]*Institute of Electrophysics, Ural Branch of the Russian Academy of Sciences, 106 Amundsena St., 620016 Ekaterinburg, Russia*
[b]*Ural Federal University named after the first President of Russia B.N. Yeltsin, 19 Mira St., 620002 Ekaterinburg, Russia*
[c]*North-Caucasus Federal University, 2 Kulakova Ave., 355099 Stavropol, Russia*
[d]*Centre de Recherche sur les Ions, les Matériaux et la Photonique (CIMAP), UMR 6252 CEA-CNRS-ENSICAEN, Université de Caen Normandie, 6 Boulevard Maréchal Juin, 14050 Caen Cedex 4, France*
**Corresponding author, e-mail: patrice.camy@ensicaen.fr*

Abstract: Compositionally "mixed" (yttria-scandia) sesquioxide transparent ceramics doped with erbium ions, ~7 at.% Er:$(Sc_xY_{1-x})_2O_3$ (where x = 0 – 0.445) were fabricated by vacuum sintering at 1750 °C for 5 h using 1.7 mol.% ZrO_2 as a sintering additive. For this, nanopowders of the same composition obtained by laser ablation and sedimentation were used. The as-prepared nanoparticles (monoclinic sp. gr. *C*2/*m*) had a mean size of 20 nm and they were transformed into the stable cubic phase by calcination at 870–1150 °C. The ceramics were of single-phase nature (C-type bixbyite structure, sp. gr. *Ia*-3). For the $(Er_{0.074}Sc_{0.114}Y_{0.812})_2O_3$ ceramic, the lattice constant was a = 10.5067 Å, the mean grain size – 21.6 μm, the average content of pores – 4.2 ppm and the transmission at 1.1 μm - 81.9%. The X-ray diffraction and Raman studies of ceramics confirmed the existence of a solid-solution composition. With increasing the Sc^{3+} content in the ceramics, their lattice shrinked, the mean grain size increased and the thermal conductivity decreased from 6.14 to 3.66 $Wm^{-1}K^{-1}$ at room temperature. The "mixed" ceramics exhibited intense inhomogeneously broadened emission around 2.8 μm making them promising for mid-infrared lasers.

Keywords: transparent ceramics; sesquioxides; erbium ion; luminescence.

1. Introduction

A substitutional solid solution represents a family of materials with a chemical formula $A_{1-x}B_x$ ($0 < x < 1$) having a single-crystal structure. Solid-solution materials are also called "mixed" indicating the mixing of components at the atomic level. If the end members (A and B, called parent materials) are isostructural, a continuous isostructural series of "mixed" materials $A_{1-x}B_x$ is formed. The formation of "mixed" compositions is common for minerals. The criteria for the existence of solid-solutions between two parents are given by the Hume-Rothery rules. "Mixed" host matrices are attractive for doping with trivalent rare-earth ions (RE^{3+}) as they exhibit inhomogeneous spectral broadening of their absorption and emission bands [1,2]. It arises from the composition variation of the nearest-neighbor cationic coordination sphere (the ligand) of the RE^{3+} ions. The broadband emission behavior of a material is of practical importance for the development of broadly tunable lasers and especially ultrafast (femtosecond) oscillators as much shorter laser pulses can be generated using RE^{3+}-doped "mixed" materials as compared to the corresponding parent ones [3-5]. However, solid-solution compositions may suffer from reduced thermal conductivity and optical quality. Thus, it is of practical importance to search for solid-solution laser host matrices combining broadband emission properties of RE^{3+} dopants with reasonable thermal behavior.

A sesquioxide (from Latin *sēsqui* – one and a half) is an oxide containing three atoms of oxygen and two atoms of another element. Cubic (sp. gr. *Ia*-3) rare-earth sesquioxides, A_2O_3 (where A = Y, Lu or Sc), are well-known as excellent host matrices for doping with various laser-active RE^{3+} ions such as Yb^{3+}, Er^{3+}, Tm^{3+}, Ho^{3+} [6]. As host materials, they feature good thermo-mechanical properties (high thermal conductivity, weak thermal expansion), broadband transparency, low phonon energies (for oxide materials) and high refractive indices. They can accommodate RE^{3+} ions in high concentrations (there exist two rare-earth sites with C_2 and C_{3i} symmetries and VI-fold oxygen coordination) [7]. The RE^{3+} ions in A_2O_3 crystals experience strong crystal-fields leading to broad emission spectra [8-10]. The rare-earth sesquoixodes can easily form solid-solutions, $(A_{1-x}B_x)_2O_3$ and $(A_{1-x-y}B_xC_y)_2O_3$ [11]. The main drawback of A_2O_3 compounds is their extremely high melting points (e.g., 2425 °C for Y_2O_3) complicating the growth of single-crystals [12,13]. Still, RE^{3+}-doped "mixed" $(Lu,Sc)_2O_3$ single-crystals were prepared [3].

Rare-earth sesquioxides are very suitable for the transparent ceramic technology [14-16]. It helps to greatly reduce the synthesis temperature (typically down to 1800±50 °C), ensures size-scalable production and simplifies the fabrication of highly-doped and especially "mixed" materials with a well-defined composition (i.e., A/B balances) and uniform dopant distribution (as there is almost no segregation of RE^{3+} ions as in the case of single-crystals). In the past years, "mixed" sesquioxide transparent ceramics $(Lu,Sc)_2O_3$, $(Lu,Y)_2O_3$ doped with various rare-earth ions such as Yb^{3+} [17-19], Tm^{3+} [20,21] or Ho^{3+} [22] were fabricated. They evidenced smooth and broad emission bands (as compared to the corresponding parent compounds) leading to generation of record-short laser pulses from mode-locked oscillators [4,5]. Note that in the series Y_2O_3 – Lu_2O_3 – Sc_2O_3, the strength of the crystal field gradually increases leading to larger Stark splitting of the RE^{3+} multiplets [8]. Thus, it is of particular interest to explore RE^{3+}-doped $(Y,Sc)_2O_3$ solid-solutions considering a significant difference of the ionic radii of Y^{3+} (0.9 Å) and Sc^{3+} (0.745 Å) for VI-fold oxygen coordination [23]. The elaboration of a cost-effective process for fabricating transparent ceramics based on the Y_2O_3–Sc_2O_3 solid-solution is a relevant task since the melt growth of high-quality $(Y_xSc_{1-x})_2O_3$ crystals with $x > 0.55$ is hindered by the hexagonal to cubic phase transition near the melting point [11,24]. In addition, the $(Y,Sc)_2O_3$ composition is more cost-effective as compared to $(Lu,Sc)_2O_3$ owing to the availability of the high-purity Y_2O_3 reagent.

Powders with sub-μm- and nm-sized particles usually serve as starting materials for manufacturing transparent ceramics. One of the most promising methods for producing oxide nanoparticles is laser ablation. It consists of evaporating a solid target material using a high-power laser, with the eventual condensation of the vapor carried out in a buffer gas flow. This method is of particular interest for solid-solution compositions, as it provides homogeneous mixing of RE-radicals followed by fast crystallization of vapors into nano-sized particles having a uniform distribution of chemical elements through their volume [25]. Moreover, high sintering activity of laser-ablated nanopowders enables to achieve full densification of green bodies by conventional vacuum sintering and to avoid costly hot isostatic pressing (HIPing) post-treatment typically used for fabricating "mixed" sesquioxide transparent ceramics with laser quality [20,21].

In the present work, we report on the synthesis, structure, vibronic and thermal behavior, as well as broadband mid-infrared (MIR) emission properties of highly Er^{3+}-doped "mixed" $(Y,Sc)_2O_3$ transparent sesquioxide ceramics with different Y/Sc balances based on laser-ablated nanopowders. Parent Er^{3+}-doped sesquioxides (both single-crystals and ceramics) are known as efficient gain media for MIR lasers operating at ~2.8 μm [26,27]. Recently, a "mixed" $Er:(Lu,Sc)_2O_3$ transparent laser ceramic with a single composition was reported [2].

2. Synthesis of nanopowders and ceramics

2.1. Synthesis of $Er:(Sc_xY_{1-x})_2O_3$ nanopowders by laser ablation

In the present work, nanopowders with a composition $Er:(Sc_xY_{1-x})_2O_3$ were obtained by laser ablation. To prepare solid targets for further laser ablation, commercial high-purity powders of Er_2O_3, Sc_2O_3 (purity: 4N, Lanhit Ltd., Russia) and Y_2O_3 (5N, Nevatorg Ltd., Russia) were weighed in the proportion $Er_{0.14}(Sc_xY_{1-x})_{1.86}O_3$ (where x = 0, 0.125, 0.25 and 0.5) and then dry mixed together for 24 hours (h) using a rotary mixer with an inclined axis of rotation. A small amount of zirconium dioxide (ZrO_2, 4N metal basis, Lanhit Ltd., Russia) was added in the mixtures as a sintering additive. The obtained blends were uniaxially pressed at 19–29 MPa into cylindrical-shaped targets with a diameter of 66 mm and a thickness of 22 mm. Then, the targets were calcined in air at 1250–1450 °C for 5 h to reach the mechanical strength sufficient for laser ablation. The applied pressure and calcination temperature were adjusted for each composition to obtain clean and crack-free targets with a relative density of at least 45%.

The calcined targets were subjected to ablation by pulsed radiation from an LS-1 diode-pumped ytterbium fiber laser (IPG Photonics) operating at a wavelength of 1070 nm. The duration and repetition rate of rectangular pulses were 120 μs and 3.5 kHz, respectively. The laser radiation with an average power of 360 W was focused into a spot with a diameter of 50 μm using an Optoskand d25 f60/200 collimating unit with a focal length of 200 mm. The power density at the target surface reached 1 MW/cm^2. Nanosized particles of complex chemical composition were synthesized as a result of laser torch vapor condensation in air flow. The detailed description of the experimental setup used for the synthesis of nanopowders can be found elsewhere [28].

2.2. Fabrication of $Er:(Sc_xY_{1-x})_2O_3$ transparent ceramics

Prior to compaction process, the coarse and shapeless particles formed through the spraying from the liquid phase by the reactive force of the ejected vapor plume were removed from the synthesized nanopowders using sedimentation [29]. The resulted fractions of nanoparticles were annealed in air at 600 °C for 3 h to burn out the residual organic components and then were uniaxially dry-pressed at 166 MPa into cylindrical green bodies with a diameter of 15 mm and a thickness of ~3 mm. Depending on the Y/Sc

balance, the relative density of pressed compacts was 43–47% considering the X-ray density of each composition. The obtained compacts were calcined in air at 900 °C for 3 h to remove residual traces of oleic acid used as a lubricating medium during uniaxial pressing. After calcination, the compacts were sintered at 1750 °C for 5 h under 10^{-5} mbar vacuum in a high temperature furnace (FIRE RAS, Russia) equipped with graphite heating elements. The sintered ceramic disks were annealed in air at 1400 °C for 2 h to eliminate color centers and then mirror-polished on both sides, see Fig. 1. The thickness of the polished disks was ~1.8 mm.

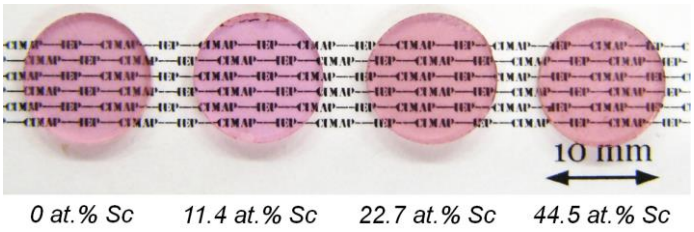

Figure 1. A photograph of annealed and polished Er:$(Sc_xY_{1-x})_2O_3$ ceramic disks.

3. Experimental

3.1. Characterization of nanopowders

The morphological features of the as-synthesized nanoparticles were observed using a JEOL JEM 2100 (JEOL Ltd., Japan) transmission electron microscope (TEM). The chemical composition of the nanopowders was analyzed using an Optima 2100 DV inductively coupled plasma mass spectrometer (ICP MS, Perkin Elmer, USA) to determine the exact Y/Sc balances and the actual Er^{3+} doping concentrations.

The phase composition of nanoparticles was studied using a D8 Discover (Bruker AXS, Germany) diffractometer in the 2θ = 20 – 60° range using Cu Kα radiation. The analysis and the Rietveld refinement of the diffraction data were carried out using the TOPAS 3.0 software.

The specific surface area (S) of nanoparticles was determined by the Brunauer-Emmett-Teller (BET) method using a TriStar 3000 gas adsorption analyzer (Micromeritics, USA). The equivalent particle diameter (d_{BET}) was then calculated using the following equation: $d_{BET} = 6/(\rho \cdot S)$, where ρ is the density of the material evaluated from the XRD analysis.

The thermal behavior of as-synthesized nanopowders was investigated in a temperature range of 20 – 1250 °C with a heating rate of 10 °C/min in air using thermogravimetry and differential thermal analysis (TG–DTA, STA 449 F5, NETZSCH, Germany).

3.2. Characterization of ceramics

The crystal structure of the sintered ceramics was characterized by an X-ray diffractometer (XRD, Empyrean, Panalytical, Netherlands) equipped with an X-ray tube with a copper anode (Cu Kα1 radiation, λ = 1.54059 Å), in the range of diffraction angles 2θ = 20 – 60°, with a step size of 0.01° and a scanning speed of 0.7 °/min. The phase identification and the full profile analysis of diffraction patterns by the Rietveld method were carried out using the Highscore Plus software with the ICDD PDF-2 database.

The morphology of the polished and thermally etched surface of the fabricated ceramic samples was observed using an optical microscope BX51TRF (Olympus, Japan). The optical micrographs were processed with the ImageJ software to determine the average grain size by the linear intercept method. Optical microscopy was also used to

evaluate the average content of scattering centers throughout the depth of the sample by means of the direct counting method [30].

To investigate the homogeneity of samples, the elemental composition of polished and thermally etched surface of ceramics was measured in three different points (a triple junction, a grain boundary and a grain interior) using a scanning electron microscope (FESEM, LM Mira 3, Tescan, Czech Republic) equipped with an elemental analysis module (EDS, X-Max 20, Oxford Instruments, UK).

The transmission spectra of ceramics were measured at room temperature over the wavelength range of 200 – 1100 nm using a UV–1700 spectrophotometer (Shimadzu Corp., Japan).

The thermal conductivity of the fabricated ceramic samples was determined using the following equation: $\kappa = \alpha C_p \rho$, where α is the thermal diffusivity, C_p is the specific heat and ρ is the density. The former two parameters were measured in the temperature range of 25–300 °C by the laser flash method using a LFA 467 HyperFlash system (NETZSCH, Germany).

The Raman spectra of ceramics were measured using a confocal Raman microscope (inVia, Renishaw) equipped with a ×50 objective (Leica) and an Ar^+ ion laser (457.0 nm).

The spectra of MIR luminescence of Er^{3+} ions were measured using an optical spectrum analyzer (Yokogawa AQ6376) purged with N_2 gas to eliminate the structured water vapor absorption in the air and a zirconium fluoride (ZrF_4) fiber. As an excitation source, a Ti:Sapphire laser (model 3900 S, Spectra Physics) tuned to 981 nm was used.

4. Results and discussion

4.1. Properties of Er:$(Sc_xY_{1-x})_2O_3$ nanoparticles synthesized by laser ablation

During the laser ablation synthesis of nanoparticles of complex composition, the target consists of a mixture of several oxides (Er_2O_3, Y_2O_3, Sc_2O_3 and ZrO_2, in our case). The rare-earth oxides composing the laser target have different melting points and absorption coefficient at the laser wavelength (1070 nm), so that the rates of evaporation of these materials are different. This determines a changed composition of the laser plume as compared to the initial composition of the target. As a result, it is necessary to determine the actual Er^{3+} doping concentration and the Y/Sc balances in the produced nanoparticles. According to the ICP MS analysis, the stoichiometric composition of the as-obtained nanopowders was the following: $(Er_{0.075}Y_{0.925})_2O_3$, $(Er_{0.074}Sc_{0.114}Y_{0.812})_2O_3$, $(Er_{0.073}Sc_{0.227}Y_{0.7})_2O_3$ and $(Er_{0.072}Sc_{0.445}Y_{0.483})_2O_3$ for x = 0, 0.125, 0.25 and 0.5, respectively.

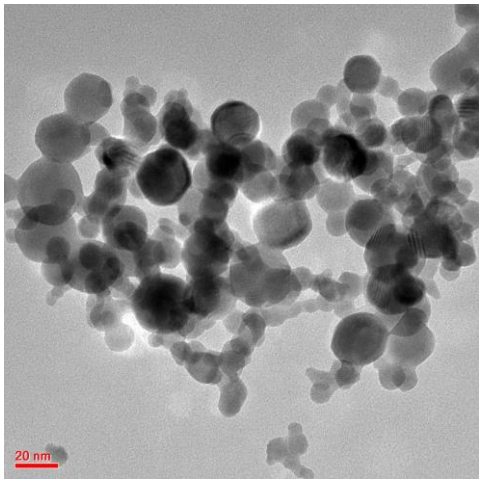

Figure 2. An example TEM image of $(Er_{0.072}Sc_{0.445}Y_{0.483})_2O_3$ nanoparticles produced by the laser ablation method.

An example TEM image of the as-obtained $(Er_{0.072}Sc_{0.445}Y_{0.483})_2O_3$ nanoparticles synthesized by laser ablation is shown in Fig. 2. The particles are weakly agglomerated mainly possessing a spherical shape. Regardless of the Sc content, their average size determined from the TEM analysis is ~20 nm. Only a slight dependence of the equivalent particle diameter determined by the BET method on the Sc content was observed, Table 1. The d_{BET} value tend to increase from 16 to 18-19 nm with increasing the Sc content. These values are in line with the TEM observations.

Figure 3 shows the X-ray diffraction (XRD) patterns of the as-synthesized Er:$(Sc_xY_{1-x})_2O_3$ nanopowders. Two crystalline phases were identified corresponding to a solid-solution of sesquioxides with a metastable monoclinic (sp. gr. *C*2/*m*) or a cubic (C-type, sp. gr. *Ia*-3) modifications of Y_2O_3 according to the ICDD cards No. 00-044-0399 and No. 00-041-1105, respectively. The lattice parameters of each phase evaluated from the XRD analysis are listed in Table 1. Usually, during the laser ablation synthesis of nanoparticles, in addition to the nanosized fraction, the as-obtained nanopowders contain a certain amount of relatively large droplets and fragments of the laser target which are not fully eliminated by the cyclone system of the used laser set-up. These foreign particles prevent the uniform packing of nanoparticles into compacts and their uniform densification leading to formation of scattering centers and deterioration of the optical quality of the final sintered ceramics which will be discussed below.

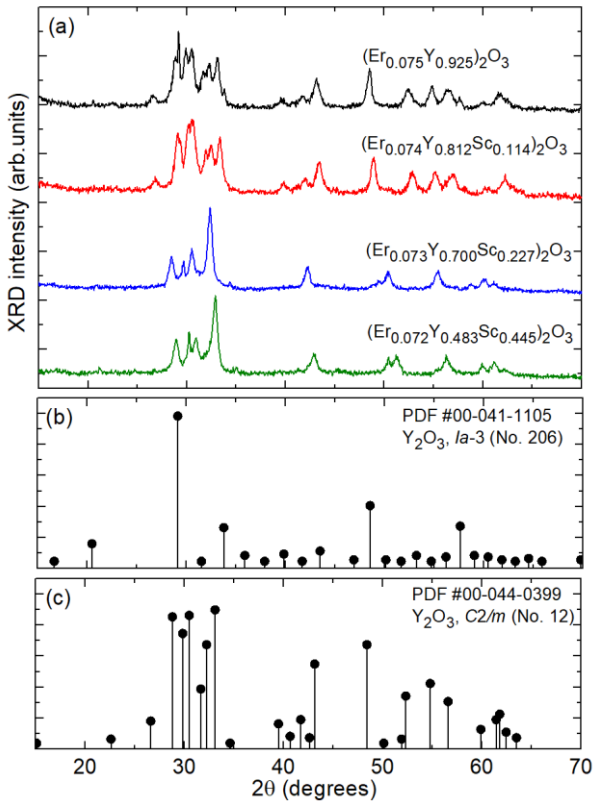

Figure 3. (a) X-ray diffractograms of the as-synthesized Er:$(Sc_xY_{1-x})_2O_3$ nanopowders with different Sc contents; (b,c) theoretical reflections for (b) cubic (sp. gr. *Ia-3*) and (c) monoclinic (sp. gr. *C*2/*m*) Y_2O_3.

Table 1. Crystal structures of the as-synthesized Er:$(Sc_xY_{1-x})_2O_3$ nanopowders.

Sample	S_{BET}, m^2/g	d_{BET}, nm	Crystal phase, sp. gr.	Content, wt.%	Lattice parameters
$(Er_{0.075}Y_{0.925})_2O_3$	66.8	15.6	Monoclinic *C2/m*	96.2	a = 13.899 Å; b = 3.497 Å; c = 8.615 Å; β = 100.32°

			Cubic *Ia-3*	3.8	a = 10.602 Å
$(Er_{0.074}Sc_{0.114}Y_{0.812})_2O_3$	61.2	17.5	Monoclinic *C2/m*	100	a = 13.840 Å; b = 3.471 Å; c = 8.661 Å; β = 100.57°
$(Er_{0.073}Sc_{0.227}Y_{0.7})_2O_3$	56.6	19.5	Monoclinic *C2/m*	91.6	a = 13.310 Å; b = 3.612 Å; c = 8.570 Å; β = 104.60°
			Cubic *Ia-3*	8.4	a = 10.430 Å
$(Er_{0.072}Sc_{0.445}Y_{0.483})_2O_3$	64.0	18.2	Monoclinic *C2/m*	85.0	A = 13.190 Å; b = 3.552 Å; c = 8.440 Å; β = 104.40°
			Cubic *Ia-3*	15.0	a = 10.240 Å

When the Er:$(Sc_xY_{1-x})_2O_3$ nanopowders are calcined in air, the DTA and H_2O ion current curves (Fig. 4) clearly show broad peaks in the range of temperatures of 100 – 300 °C due to the loss of adsorbed moisture and water of crystallization. The weight decrease in this temperature range reaches 3.5–4.5%, which is more than half of the total weight loss registered at 1250 °C. An exothermic process of decomposition of organic compounds proceeds in the range of 370–410 °C with the release of carbon dioxide, which is clearly observed in the CO_2 ion current curve. An exothermic process of particle phase conversion from the monoclinic into the cubic modification occurs at a temperature of 870–1150 °C depending on the composition of the sample. With increasing the Sc content, the onset of the phase transformation gradually shifts towards higher temperatures.

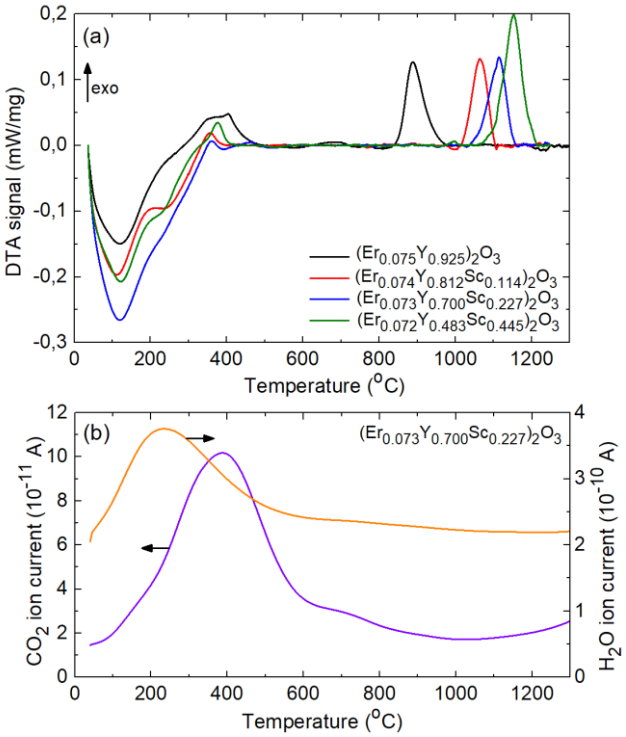

Figure 4. (a) DTA curves showing the thermal behavior of Er:$(Sc_xY_{1-x})_2O_3$ nanopowders; (b) CO_2 and H_2O ion current curves for the sample $(Er_{0.073}Sc_{0.227}Y_{0.7})_2O_3$.

4.2. Structural properties of Er:$(Sc_xY_{1-x})_2O_3$ transparent ceramics

Figure 5(a) presents the XRD patterns of the obtained transparent Er:$(Sc_xY_{1-x})_2O_3$ ceramics with different Sc contents. The diffraction peaks can be well interpreted assuming a single-phase sesquioxide solid-solution with a cubic bixbyite structure (C-type, sp. gr. *Ia-3*) which most closely corresponds to the cubic Y_2O_3 phase in terms of the positions and relative intensities of the diffraction peaks (ICSD pattern No. 01-086-1326), Fig. 5(b). No

secondary phases relative to the presence of ZrO_2 as a sintering additive are detected. With increasing the Sc content, the diffraction peaks shift towards larger diffraction angles, see Fig. 5(c,d) highlighting the most intense (222) reflection of the cubic sesquioxide structure. This confirms the formation of a solid-solution between yttria (Y_2O_3, *a* = 10.604 Å) and scandia (Sc_2O_3, *a* = 9.845 Å). The refinement of the structure using a full-profile analysis of the XRD patterns by the Rietveld method indicated that the lattice parameter of ceramics decreases linearly with increasing the Sc content according to the Vegard's law. For the samples containing 0, 11.4 at.%, 22.7 at.% and 44.5 at.% Sc^{3+}, *a* = 10.5947 Å, 10.5067 Å, 10.4211 Å and 10.2421 Å, respectively.

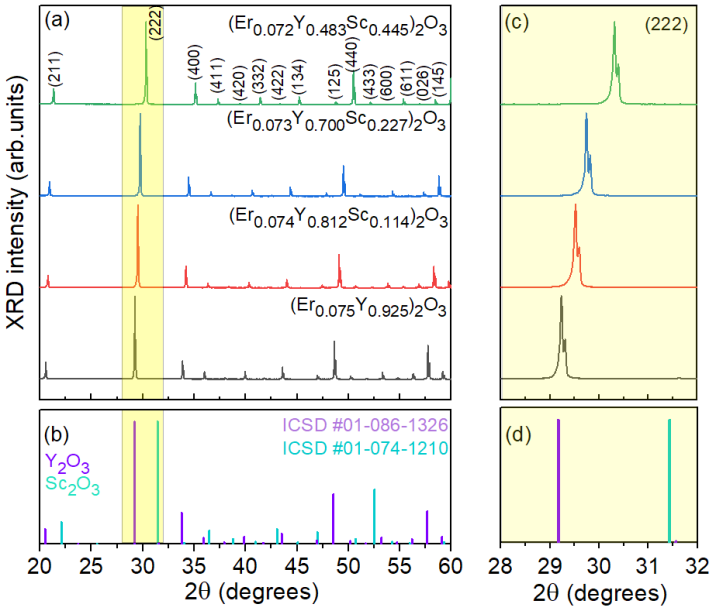

Figure 5. (a) X-ray diffraction (XRD) patterns of the as-sintered Er:$(Sc_xY_{1-x})_2O_3$ ceramics, *numbers* – Miller's indices (*hkl*); (b) theoretical XRD patterns of Y_2O_3 (ICSD card No. 01-086-1326) and Sc_2O_3 (ICSD card No. 01-074-1210); (c) a close look on the (222) reflection of the sesquioxide phase; (d) the corresponding theoretical reflections of Y_2O_3 and Sc_2O_3.

The surface morphology of the obtained Er:$(Sc_xY_{1-x})_2O_3$ ceramics after polishing and thermal etching is shown in Fig. 6. The sintered samples consist of tightly-packed micro-crystallites with polyhedral shape separated by clean and well-defined grain boundaries. The average grain size increases from 9.6 μm for the Er:Y_2O_3 ceramic to 21.6 μm, 23.5 μm and 24.7 μm for those containing 11.4 mol%, 22.7 mol% and 44.5 mol% of Sc_2O_3, respectively. The spherical pores exhibiting a characteristic size of 2–5 μm are relatively homogeneously distributed throughout the depth of the ceramics, see the insets in Fig. 6, and their average content is 3.2 ppm, 4.2 ppm, 31.4 ppm and 33.8 ppm for the $(Er_{0.075}Y_{0.925})_2O_3$, $(Er_{0.074}Sc_{0.114}Y_{0.812})_2O_3$, $(Er_{0.073}Sc_{0.227}Y_{0.7})_2O_3$ and $(Er_{0.072}Sc_{0.445}Y_{0.483})_2O_3$ ceramics, respectively.

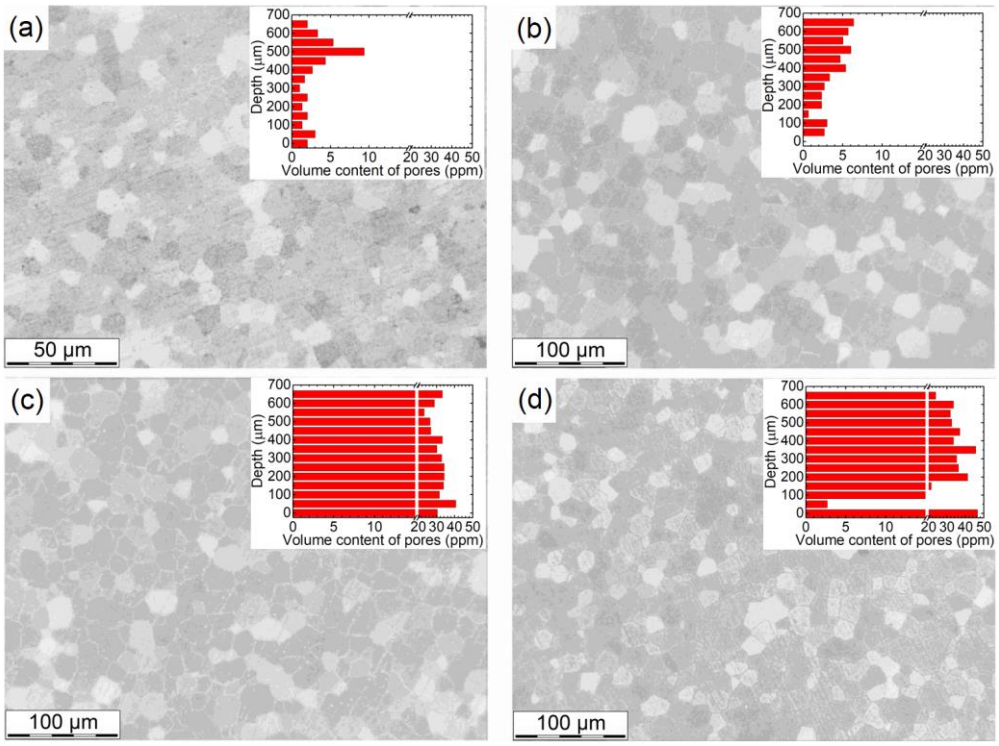

Figure 6. (a-d) Optical microscopy images of polished and thermally etched surface of ceramic disks: (a) $(Er_{0.075}Y_{0.925})_2O_3$; (b) $(Er_{0.074}Sc_{0.114}Y_{0.812})_2O_3$; (c) $(Er_{0.073}Sc_{0.227}Y_{0.7})_2O_3$; (d) $(Er_{0.072}Sc_{0.445}Y_{0.483})_2O_3$. *Insets* – the distributions of scattering centers across the depth of ceramics.

Table 2 presents the chemical composition of the ceramic samples determined using energy dispersive spectroscopy (EDS) analysis in three different points depicted in Fig. 7(a-d). The Er, Y and Sc contents were nearly constant between the grains, grain boundaries and triple junctions. Consequently, it can be concluded that the homogeneity of the distribution of components previously achieved in laser-ablated nanopowders is retained in the sintered ceramics.

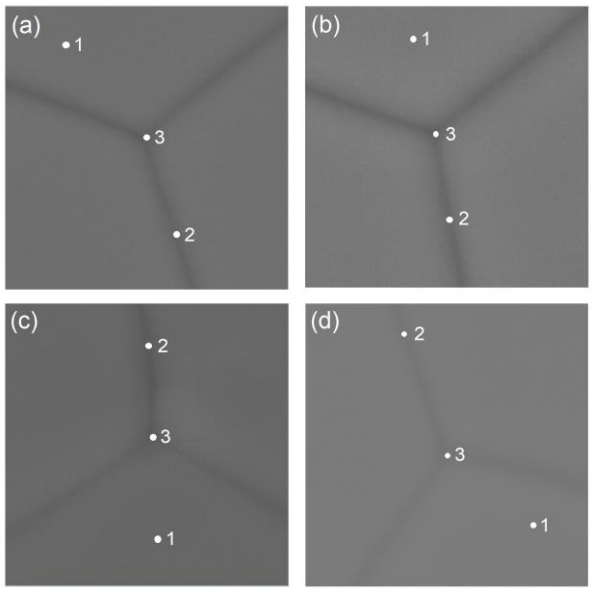

Figure 7. (a-d) SEM images showing three different spots selected for the EDS analysis of chemical composition of the studied ceramics: (a)

$(Er_{0.075}Y_{0.925})_2O_3$; (b) $(Er_{0.074}Sc_{0.114}Y_{0.812})_2O_3$; (c) $(Er_{0.073}Sc_{0.227}Y_{0.7})_2O_3$; (d) $(Er_{0.072}Sc_{0.445}Y_{0.483})_2O_3$.

Table 2. EDS-based compositional analysis of grains (spot 1), grain boundaries (spot 2) and triple junctions (spot 3) in the Er:$(Sc_xY_{1-x})_2O_3$ ceramics.

Spot number	Er (wt.%)	Y (wt.%)	Sc (wt.%)	Zr (wt.%)	O (wt.%)
$(Er_{0.075}Y_{0.925})_2O_3$					
1	10.16	72.56	-	1.40	15.88
2	9.84	71.60	-	1.21	17.35
3	9.86	71.63	-	1.33	17.18
$(Er_{0.074}Sc_{0.114}Y_{0.812})_2O_3$					
1	10.80	64.80	5.22	1.49	17.68
2	10.77	65.26	5.29	1.48	17.20
3	10.80	64.80	5.22	1.49	17.68
$(Er_{0.073}Sc_{0.227}Y_{0.7})_2O_3$					
1	10.33	55.48	10.10	1.66	22.43
2	10.62	57.92	10.49	1.62	19.35
3	10.57	57.63	10.47	1.69	19.63
$(Er_{0.072}Sc_{0.445}Y_{0.483})_2O_3$					
1	11.03	41.61	23.24	1.64	22.47
2	11.22	42.14	23.72	1.45	21.47
3	11.14	41.96	23.70	1.61	21.59

4.3. Raman spectra of Er:$(Sc_xY_{1-x})_2O_3$ transparent ceramics

The Raman spectra of the Er:$(Sc_xY_{1-x})_2O_3$ transparent ceramics are shown in Fig. 8. They were measured for λ_{exc} = 457 nm to avoid overlap with the Er^{3+} luminescence. For cubic (C-type) Y_2O_3 with a body-centered structure, the factor group analysis predicts the following irreducible representations for the optical and acoustical modes at the Γ-point (***k*** = 0): $\Gamma_{op} = 4A_g + 4E_g + 14F_g + 5A_{2u} + 5E_u + 16F_u$, $\Gamma_{ac} = F_u$, of which 22 modes (A_g, E_g and F_g) are Raman-active, 16 modes (F_u) are IR-active and the rest are silent [9,31]. The measured spectra are characteristic for cubic sesquioxides. For the $(Er_{0.075}Y_{0.925})_2O_3$ ceramic, a total of 12 modes are observed: ~128, 159, 192, 259, 318, 330, 378, 431, 470, 537, 566 and 594 cm^{-1}. The most intense mode at 377.5 cm^{-1} (linewidth: FWHM = 11 cm^{-1}) is assigned to A_g + F_g vibrations. With increasing the Sc^{3+} content in the ceramics, the Raman spectra notably broaden and the positions of the prominent Raman peaks shift to larger energies. E.g., for the ceramics with 0 at.% Sc^{3+}, 11.4 at.% Sc^{3+}, 22.7 at.% Sc^{3+} and 44.5 at.% Sc^{3+}, the most intense Raman peak is observed at 377.5, 383.8, 388.9 and 398.4 cm^{-1}, respectively. For the latter ceramic, the linewidth of this peak increases to 43 cm^{-1}. This behavior well agrees with the phonon spectra of the parent compounds showing the most intense peaks at 376 cm^{-1} (Y_2O_3) and 419 cm^{-1} (Sc_2O_3) and indicated a formation of a solid-solution rather than a mixture of two separate cubic sesquioxide phases. A similar behavior for certain “mixed” polycrystalline sesquioxides was observed previously [32].

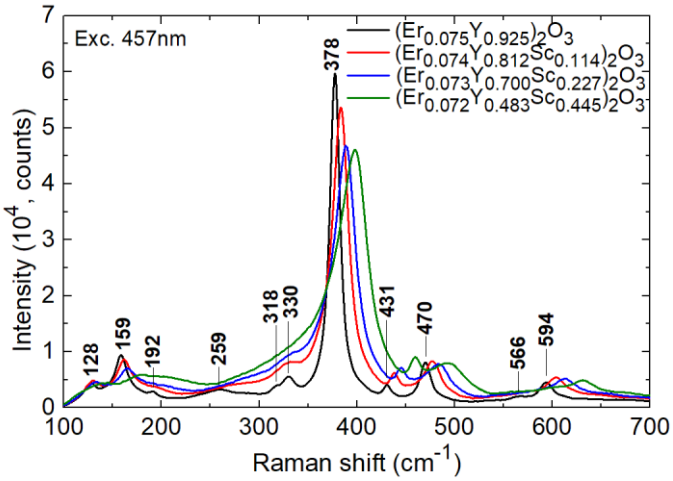

Figure 8. Raman spectra of Er:$(Sc_xY_{1-x})_2O_3$ ceramics, *numbers* – peak Raman frequencies, λ_{exc} = 457 nm.

4.4. Transmission of Er:$(Sc_xY_{1-x})_2O_3$ transparent ceramics

The in-line transmission spectra of the annealed Er:$(Sc_xY_{1-x})_2O_3$ ceramics with a thickness of 1.8 mm are shown in Fig. 9. The spectra exhibit absorption band characteristic for Er^{3+} ions. The ceramic with a parent composition Er:Y_2O_3 possesses the highest transmission T of 83.1±1% at the wavelength of 1100 nm (out of Er^{3+} absorption). The theoretical transmission T_0 of pure Y_2O_3 and Sc_2O_3 ceramics can be calculated using the refractive index data reported by Kaminskii *et al.* [33,34] and a modified Fresnel equation accounting for multiple light reflections at the sample interfaces: $T_0 = 2n/(n^2 + 1)$, where n is the refractive index at the wavelength of interest. Consequently, the theoretical value was estimated to be 82.7% for Y_2O_3 and 81.0% for Sc_2O_3 at 1100 nm and the transmission measured for Sc^{3+}-doped ceramics reaches these limits except of the sample $(Er_{0.072}Sc_{0.445}Y_{0.483})_2O_3$ for which T is only 79.2%. The measured values of transmission for different ceramics correlate with the corresponding average content of pores acting as scattering centers, see the insets in Fig. 6. A notable drop-off in transmission in the visible spectral range can be attributed to remnant porosity.

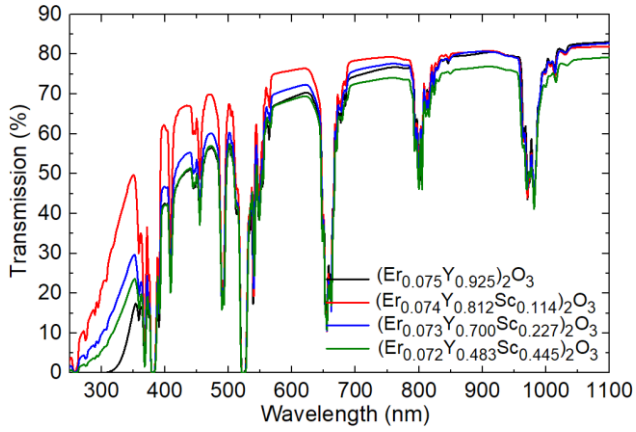

Figure 9. Transmission spectra of the fabricated Er:$(Sc_xY_{1-x})_2O_3$ transparent ceramics.

4.5. Thermal conductivity of Er:$(Sc_xY_{1-x})_2O_3$ transparent ceramics

The values of thermal diffusivity and specific heat capacity of the synthesized Er:$(Sc_xY_{1-x})_2O_3$ ceramics at room temperature measured by the laser flash method along with the calculated thermal conductivities are listed in Table 3. With increasing the Sc

content in the ceramics from 0 to 44.5 at.%, the room temperature thermal conductivity gradually decreases from 6.14 to 3.66 $Wm^{-1}K^{-1}$, as expected for solid-solution compositions. According to the temperature dependences shown in Fig. 10, a temperature rise up to 300 °C also leads to a reduction in thermal conductivity of the samples by about 27%.

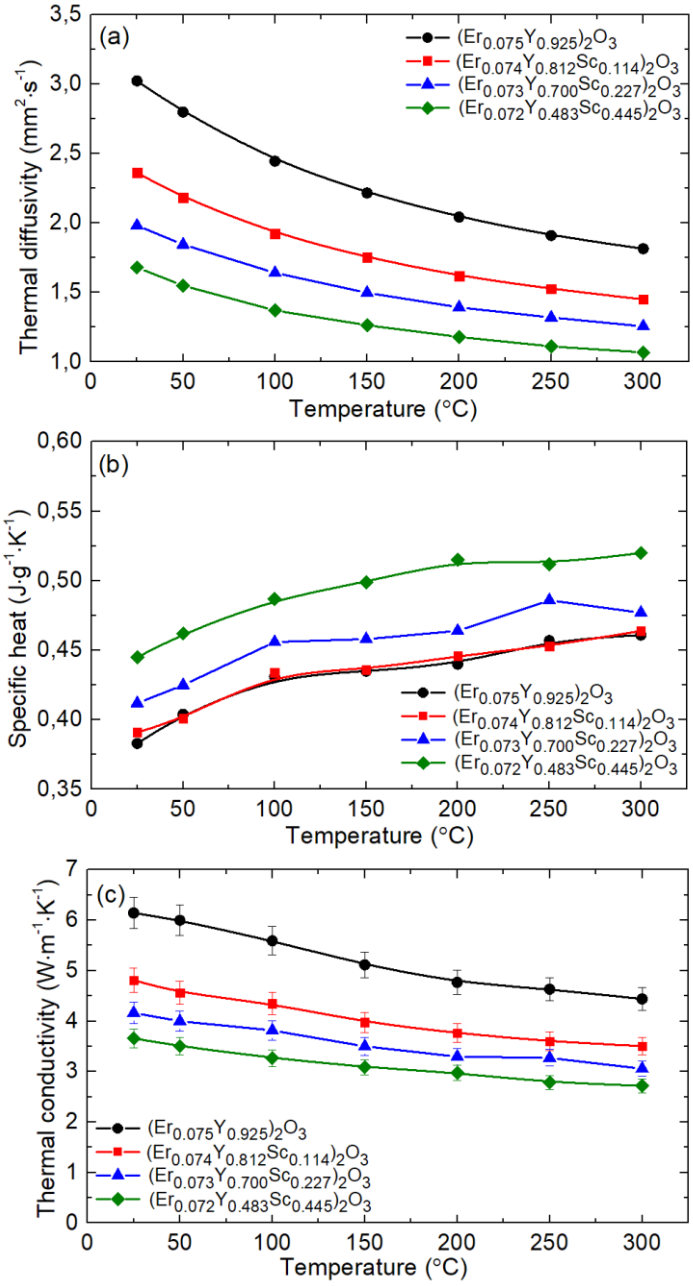

Figure 10. Dependences of (a) thermal diffusivity, (b) specific heat and (c) thermal conductivity on the temperature for the obtained Er:$(Sc_xY_{1-x})_2O_3$ ceramic samples.

Table 3. Thermal properties of ~7 at.% Er:$(Sc_xY_{1-x})_2O_3$ transparent ceramics with various Sc contents at room temperature. The samples also contain about 1.7 mol.% ZrO_2 as a sintering additive.

Sc content, at.%	Thermal diffusivity, mm^2/s	Specific heat capacity, $Jg^{-1}K^{-1}$	Density, g/cm^3	Thermal conductivity, $Wm^{-1}K^{-1}$
0	3.023	0.383	5.307	6.14
11.4	2.362	0.391	5.208	4.81

22.7	1.982	0.412	5.100	4.16
44.5	1.680	0.445	4.895	3.66

4.6. Mid-infrared luminescence of Er^{3+} ions

The spectra of MIR luminescence of Er^{3+} ions in the Er:$(Sc_xY_{1-x})_2O_3$ ceramics (water vapor absorption excluded) are shown in Fig. 11(a). The spectra are broad spanning from 2.55 to 3.1 μm; the luminescence is assigned to the $^4I_{11/2} \rightarrow {}^4I_{13/2}$ Er^{3+} transition. With increasing the Sc^{3+} content in the ceramics, the spectra are notably broadened. For the $(Er_{0.075}Y_{0.925})_2O_3$ ceramic, the spectrum contains several narrow intense peaks at 2710, 2717, 2725 and 2740 nm and a broad less intense band at 2842 nm (FWHM = 22 nm) usually used for achieving laser operation due to the weaker overlap with the structured water vapor absorption in the air. For the $(Er_{0.072}Sc_{0.445}Y_{0.483})_2O_3$ ceramic, the spectrum contains a broad structured band with a maximum at 2716 nm and another less intense band centered at 2848 nm with increased FWHM of 34 nm. Figure 11(b) focuses on the spectral range of 2820–2910 nm indicating a continuous red-shift of the long-wavelength Er^{3+} emission band with increasing the Sc^{3+} content in the ceramic. It agrees well with the increase of the crystal field strength between Y_2O_3 and Sc_2O_3.

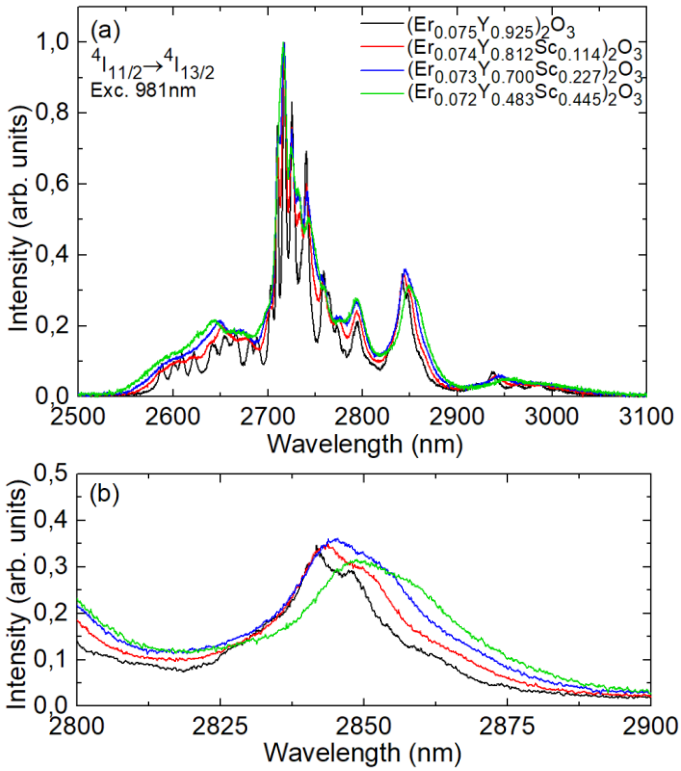

Figure 11. (a,b) MIR luminescence spectra of Er^{3+} ions in the Er:$(Sc_xY_{1-x})_2O_3$ transparent ceramics, (a) full spectra, (b) a close look at the 2800-2900 nm range, λ_{exc} = 981 nm.

4.7. Discussion

The closeness of the characteristic diameters of laser-ablated “mixed” sesquioxide nanoparticles with different Y/Sc balances (cf. Table 1) is due to the equality of the volumes of the evaporated target material per unit volume of the laser plume. Indeed, the volume of the laser plume increases until the pressure inside is balanced by the pressure of the surrounding gas. Under the used conditions of laser synthesis, the gas pressure in the chamber was constant (ambient pressure), so that the pressure inside the plume at the final

stage during steam condensation was the same, which determined the similarity in the nanoparticle diameters.

One of the features of the laser synthesis is that nanoparticles based on rare-earth sesquioxides crystallize in the metastable monoclinic phase (B-phase). For instance, B-modification of Y_2O_3 was previously observed under a pressure of 2.1 GPa at 1273 K [35]. Such a high pressure probably appears owing to electrostatic forces near oxygen vacancies which are certainly present in the monoclinic lattice [36]. It follows that the stability of the monoclinic phase under ambient conditions is determined by oxygen deficiency and a necessary condition for the B → C (monoclinic to cubic) phase transformation is the saturation of nanoparticles with oxygen to a content close to the stoichiometric composition. Another condition for the phase transformation is the formation of seed domains and their growth to a critical size so that the onset temperature increases with increasing the Sc content due to the suppression of cation diffusion [37].

A high degree of dispersion, a narrow particle size distribution and an absence of hard agglomerates in the powders are essential conditions for obtaining fully dense transparent ceramic materials by pressureless sintering during a reasonable time. The appearance of relatively large particles (up to several tens of μm) of melt droplets and porous fragments of the laser target in the as-synthesized powders is most probably associated with not enough developed cyclone system of our home-made laser set-up. The presence of coarse aggregates in the pressed powders even at low content induces inhomogeneous densification and formation of structural defects leading to deterioration of the optical quality. Note that ceramics sintered from the as-synthesized powders were opaque or translucent due to irregularities in their microstructure. The unwanted coarse fraction could be efficiently extracted from the powders via sedimentation in ethyl alcohol as the peaks corresponding to the traces of cubic phase were absent in the diffraction patterns (not shown here).

Both yttria and scandia possesses a body-centered cubic bixbyite structure (usually labeled as a C-type) and belong to the cubic space group *Ia-3* [24]. According to the previously reported phase diagram of the Y_2O_3-Sc_2O_3 binary system [38], a substitutional solid solution $(Y_xSc_{1-x})_2O_3$ with a C-type structure was observed within the whole range of $0 < x < 1$. Note that an orthorhombic perovskite yttrium scandate phase with the space group *Pnma* can be also formed under certain experimental conditions. A partial transformation into the orthorhombic $YScO_3$ phase was observed in the corresponding mixture of sesquioxides after calcination at 1650 °C under ambient pressure for 9.5 h [38] and pure perovskite modification could be obtained by firing in air at 1000 °C under 20 kbar for 1 h [39]. In addition, pure perovskite $YScO_3$ was successfully prepared using specific synthesis methods including the method of heterophase interaction, the method of co-precipitation from hydroxides and the polymerized complex method [40,41]. However, this compound is unstable and converts into a C-type Y_2O_3-Sc_2O_3 solid-solution at the temperatures above 1750 °C [38]. Despite the monoclinic structure of the laser-ablated nanoparticles used in this work, the obtained $Er:(Sc_xY_{1-x})_2O_3$ ceramics vacuum sintered at 1750 °C for 5 h are of cubic single-phase nature as identified by the XRD analysis. The ionic radii of Sc^{3+} and Y^{3+} for VI-fold oxygen coordination are 0.745 Å and 0.9 Å, respectively [23]. Therefore, incorporation of Sc^{3+} cations at the Y^{3+} sites induces a significant distortion of the crystal structure and formation of compressive strains randomly distributed throughout the lattice. The absence of additional diffraction peaks belonging to possible impurity phases determines a complete dissolution of Sc_2O_3, Er_2O_3 as well as ZrO_2 in the Y_2O_3 matrix.

Pressureless densification of “pure” rare-earth sesquioxides to full density is difficult due to separation of pores from grain boundaries caused by an enhanced grain growth at the final sintering stage [42]. The trapped intagranular pores could not be eliminated even at high temperatures and reasonably long isothermal soaking as the mass transfer in the bulk

occurs much slower than along the grain boundaries where the defect concentration is considerably higher. Special sintering additives inhibiting rapid grain growth or pressure-assisted densification methods such as hot isostatic pressing (HIPing) and spark plasma sintering (SPS) are usually employed to avoid the unwanted phenomenon. Incorporation of heterovalent sintering additives increases the concentration of defects and intensifies the diffusion flows of cations or anions. In particular, when ZrO_2 is introduced into Y_2O_3, the oxygen stoichiometry is violated so that the concentration of oxygen vacancies increases. Negatively charged cation vacancies are formed to neutralize the extra positive charge. The increase of the concentration of cationic vacancies above their thermodynamically equilibrium content increases the rate of mass transfer. In the case of soluble isovalent Sc^{3+} (Er^{3+}) additives exhibiting smaller ionic radii as compared to Y^{3+}, a partial substitution leads to a significant disorder of the crystal lattice resulting in acceleration of diffusion processes and an increase in the grain size with respect to the parent Er:Y_2O_3 composition.

Considering the presence of ~1.7 mol.% ZrO_2 in the fabricated ceramics, the thermal conductivity of 6.14±0.31 $Wm^{-1}K^{-1}$ for the $(Er_{0.075}Y_{0.925})_2O_3$ ceramic sample is comparable with the previously reported values of 7.05 $Wm^{-1}K^{-1}$ for a $(Yb_{0.08}Y_{0.92})_2O_3$ single-crystal and 6.39 $Wm^{-1}K^{-1}$ for a $(Yb_{0.08}Y_{0.89}Zr_{0.03})_2O_3$ ceramic, respectively [43,44]. Since the atomic mass and the ionic radius of Er^{3+} are close to those of Yb^{3+}, a similar level of disorder and effect on the thermal properties could be expected upon partial substitution of Y^{3+} cations by Er^{3+} or Yb^{3+} ones in the Y_2O_3 host matrix. In addition, the measured value of 3.66±0.18 $Wm^{-1}K^{-1}$ for the $(Er_{0.072}Sc_{0.445}Y_{0.483})_2O_3$ ceramic is only slightly lower than that previously reported for a single-crystal with a relatively close composition $(Er_{0.07}Sc_{0.50}Y_{0.43})_2O_3$, κ = 4.1 $Wm^{-1}K^{-1}$ [11], indicating only slightly higher concentration of lattice defects in the sintered ceramics. Oxygen vacancies formed for charge compensation owing to introducing tetravalent Zr into Y^{3+} sites could be responsible for additional drop-off in thermal conductivity. In general, it is the phonon propagation that determines the heat transport in dielectric materials and the most important parameter controlling the thermal conductivity is the mean phonon free path. The addition of Sc_2O_3 to Er:Y_2O_3 induces structural distortion because of the significant mismatch of the atomic mass and ionic radius between Sc^{3+} and Y^{3+}. The introduced Sc^{3+} cations can be considered as substitutional defects causing additional phonon scattering that shortens their mean free paths and deteriorates the thermal properties.

5. Conclusions

To conclude, a combination of laser ablation followed by sedimentation for obtaining sesquioxide nanopowders (particle size: ~20 nm) of complex composition $(Er,Y,Sc)_2O_3$ together with vacuum sintering at 1750 °C for 5 h using ZrO_2 as a sintering additive is a viable route for fabricating single-phase, high optical quality, close-packed transparent sesquioxide ceramics Er:$(Sc_xY_{1-x})_2O_3$ (where x = 0 – 0.445). As both the Er^{3+} doping and the mixture of the host-forming cations (Y^{3+} and Sc^{3+}) occur at the stage of nanopowder synthesis, high homogeneity of ceramics is achieved (note that a strong gradient of rare-earth ions is a usual problem for Sc-containing sesquioxide single crystals). The addition of Sc^{3+} has a significant effect on the material properties of ceramics: (i) the lattice parameter shrinks according to a formation of a solid-solution; (ii) the frequency of the most intense Raman mode increases and it is notably broadened; (iii) the mean grain size increases; (iv) the transmission drops only for high Sc^{3+} doping levels (x > 0.227) due to larger amount of pores probably resulted from a rapid grain growth and (v) the thermal conductivity of ceramics moderately decrease still representing a reasonably value for potential laser applications. In terms of mid-infrared emission properties of Er^{3+} ions in the “mixed” ceramics, intense and inhomogeneously broadened spectra are observed. A combination of well-preserved optical and thermal properties, as well as broadband emission from

“mixed” Er:$(Sc_xY_{1-x})_2O_3$ ceramics make them promising for the development of mid-infrared lasers emitting at ~2.8 μm.

Acknowledgements

The reported study was funded by RFBR (Russia) according to the research project No. 21-53-15014 and CNRS (France) according to the project IEA No. 00432. The thermal behaviors (TG-DTA) of the as-synthesized nanopowders were studied at the "Geoanalitik" shared research facilities of the IGG UB RAS. The re-equipment and comprehensive development of the "Geoanalitik" shared research facilities of the IGG UB RAS is financially supported by the grant of the Ministry of Science and Higher Education of the Russian Federation (Agreement No. 075-15-2021-680). The XRD, EDS and thermal properties of ceramics were studied using the equipment of the Center for Collective Use of the North-Caucasus Federal University financially supported by the Ministry of Education and Science of Russia, unique project identifier RF - 2296.61321X0029 (agreement No. 075-15-2021-687). R. M. wishing to thank Dr. A.N. Orlov (IEP UrB RAS) for the measurements of transmission spectra. P. L. also acknowledges the support from the “RELANCE” Chair of Excellence project funded by the Normandy Region.

References

1. W. Jing, P. Loiko, J.M. Serres, Y. Wang, E. Vilejshikova, M. Aguiló, F. Díaz, U. Griebner, H. Huang, V. Petrov, X. Mateos, Synthesis, spectroscopy, and efficient laser operation of “mixed” sesquioxide Tm:$(Lu,Sc)_2O_3$ transparent ceramics, Opt. Mater. Express 7 (2017) 4192-4202.
2. L. Basyrova, P. Loiko, W. Jing, Y. Wang, H. Huang, M. Aguiló, F. Díaz, E. Dunina, A. Kornienko, B. Viana, U. Griebner, V. Petrov, X. Mateos, and P. Camy, “Spectroscopy and efficient laser operation around 2.8 μm of Er:$(Lu,Sc)_2O_3$ sesquioxide ceramics,” J. Lumin. 240, 118373-1-11 (2021).
3. A. Schmidt, V. Petrov, U. Griebner, R. Peters, K. Petermann, G. Huber, C. Fiebig, K. Paschke, G. Erbert, Diode-pumped mode-locked Yb:$LuScO_3$ single crystal laser with 74 fs pulse duration, Opt. Lett. 35 (2010) 511-513.
4. Y. Wang, W. Jing, P. Loiko, Y. Zhao, H. Huang, X. Mateos, S. Suomalainen, A. Härkönen, M. Guina, U. Griebner, V. Petrov, Sub-10 optical-cycle passively mode-locked Tm:$(Lu_{2/3}Sc_{1/3})_2O_3$ ceramic laser at 2 μm, Opt. Express 26 (2018) 10299-10304.
5. Y. Zhao, L. Wang, Y. Wang, J. Zhang, P. Liu, X. Xu, Y. Liu, D. Shen, J.E. Bae, T.G. Park, F. Rotermund, X. Mateos, P. Loiko, Z. Wang, X. Xu, J. Xu, M. Mero, U. Griebner, V. Petrov, W. Chen, SWCNT-SA mode-locked Tm:$LuYO_3$ ceramic laser delivering 8-optical-cycle pulses at 2.05 μm, Opt. Lett. 45 (2020) 459-462.
6. C. Kränkel, Rare-earth-doped sesquioxides for diode-pumped high-power lasers in the 1-, 2-, and 3-μm spectral range, IEEE J. Sel. Top. Quantum Electron. 21 (2014) 250-262.
7. N. C. Chang, J. B. Gruber, R. P. Leavitt, C. A. Morrison, Optical spectra, energy levels, and crystal-field analysis of tripositive rare-earth ions in Y_2O_3. I. Kramers ions in C_2 sites, J. Chem. Phys. 76 (1982) 3877–3889.
8. P. Loiko, P. Koopmann, X. Mateos, J. M. Serres, V. Jambunathan, A. Lucianetti, T. Mocek, M. Aguiló, F. Díaz, U. Griebner, V. Petrov, C. Kränkel, Highly-efficient, compact Tm^{3+}:RE_2O_3 (RE = Y, Lu, Sc) sesquioxide lasers based on thermal guiding, IEEE J. Sel. Top. Quantum Electron. 24 (2018) 1600713-1-13.
9. L. Laversenne, Y. Guyot, C. Goutaudier, M.T. Cohen-Adad, G. Boulon, Optimization of spectroscopic properties of Yb^{3+}-doped refractory sesquioxides: cubic Y_2O_3, Lu_2O_3 and monoclinic Gd_2O_3, Opt. Mater. 16 (2001) 475-483.
10. P. Koopmann, S. Lamrini, K. Scholle, M. Schäfer, P. Fuhrberg, G. Huber, Holmium-doped Lu_2O_3, Y_2O_3, and Sc_2O_3 for lasers above 2.1 μm, Opt. Express 21 (2013) 3926-3931.
11. C. Kränkel, A. Uvarova, É. Haurat, L. Hülshoff, M. Brützam, C. Guguschev, S. Kalusniak, D. Klimm, Czochralski growth of mixed cubic sesquioxide crystals in the ternary system Lu_2O_3–Sc_2O_3–Y_2O_3, Acta. Crystallogr. B. Struct. Sci. Cryst. Eng. Mater. 77 (2021) 550-558.

12. L. Fornasiero, E. Mix, V. Peters, K. Petermann, G. Huber, Czochralski growth and laser parameters of RE^{3+}-doped Y_2O_3 and Sc_2O_3, Ceram. Int. 26 (2000) 589-592.
13. A. Fukabori, V. Chani, K. Kamada, T. Yanagida, Y. Yokota, F. Moretti, N. Kawaguchi, A. Yoshikawa, Growth of Y_2O_3, Sc_2O_3 and Lu_2O_3 crystals by the micro-pulling-down method and their optical and scintillation characteristics, J. Cryst. Growth 318 (2011) 823-827.
14. J. Lu, K. Takaichi, T. Uematsu, A. Shirakawa, M. Musha, K.I. Ueda, H. Yagi, T. Yanagitani, A.A. Kaminskii, Yb^{3+}:Y_2O_3 ceramics–a novel solid-state laser material, Jpn. J. Appl. Phys. 41 (2002) L1373-L1375.
15. J. Lu, J. F. Bisson, K. Takaichi, T. Uematsu, A. Shirakawa, M. Musha, K. Ueda, H. Yagi, T. Yanagitani, A. A. Kaminskii, Yb^{3+}:Sc_2O_3 ceramic laser, Appl. Phys. Lett. 83 (2003) 1101-1103.
16. K. Takaichi, H. Yagi, A. Shirakawa, K. Ueda, S. Hosokawa, T. Yanagitani, A.A. Kaminskii, Lu_2O_3:Yb^{3+} ceramics–a novel gain material for high-power solid-state lasers, Phys. Status Solidi A. 202 (2005) R1-R3.
17. W. Liu, H. Kou, J. Li, B. Jiang, Y. Pan, Transparent Yb:$(Lu_xSc_{1-x})_2O_3$ ceramics sintered from carbonate co-precipitated powders, Ceram. Int. 41 (2015) 6335-6339.
18. G. Toci, A. Pirri, B. Patrizi, R.N. Maksimov, V.V., Osipov, V.A. Shitov, M. Vannini, Yb^{3+}:$(Lu_xY_{1-x})_2O_3$ mixed sesquioxide ceramics for laser applications. Part II: Laser performances, J. Alloys Compd. 853 (2020) 156943.
19. W. Jing, P. Loiko, L. Basyrova, Y. Wang, H. Huang, P. Camy, U. Griebner, V. Petrov, J. M. Serres, M. Aguiló, F. Díaz, X. Mateos, Synthesis, spectroscopy and laser operation of highly-doped "mixed" 10 at.% Yb:$(Lu,Sc)_2O_3$ ceramics, Opt. Mater. 117 (2021) 111128-1-7.
20. H. Wu, G.H. Pan, Z. Hao, L. Zhang, X. Zhang, L. Zhang, H. Zhao, J. Zhang, Laser-quality Tm:$(Lu_{0.8}Sc_{0.2})_2O_3$ mixed sesquioxide ceramics shaped by gelcasting of well-dispersed nanopowders. J. Am. Ceram. Soc. 102 (2019) 4919-4928.
21. N. Zhang, Z. Wang, S. Liu, W. Jing, H. Huang, Z. Huang, K. Tian, Z. Yang, Y. Zhao, U. Griebner, V. Petrov, W. Chen, Watt-level femtosecond Tm-doped "mixed" sesquioxide ceramic laser in-band pumped by a Raman fiber laser at 1627 nm, Opt. Express 30 (2022) 23978-23985.
22. W. Jing, P. Loiko, J.M. Serres, Y. Wang, E. Vilejshikova, X. Mateos, M. Aguiló, F. Díaz, U. Griebner, H. Huang, V. Petrov, Synthesis, spectroscopy and laser operation of "mixed" Ho:$(Lu,Sc)_2O_3$ ceramics, J. Lumin. 203 (2018) 145-151.
23. R.D. Shannon, Revised effective ionic radii and systematic studies of interatomic distances in halides and chalcogenides, Acta Cryst. A32 (1976) 751–767.
24. M. Zinkevich, Thermodynamics of rare earth sesquioxides, Prog. Mater. Sci. 52 (2007) 597–647.
25. R.N. Maksimov, V.A. Shitov, V.V. Platonov, A.S. Yurovskikh, G. Toci, B. Patrizi, M. Vannini, A. Pirri, Hot isostatic pressing of transparent Yb^{3+}-doped Lu_2O_3 ceramics for laser applications, Ceram. Int. 47 (2021) 5168–5176.
26. T. Li, K. Beil, C. Kränkel, G. Huber, Efficient high-power continuous wave Er:Lu_2O_3 laser at 2.85 μm, Opt. Lett. 37 (2012) 2568-2570.
27. W. Yao, H. Uehara, S. Tokita, H. Chen, D. Konishi, M. Murakami, R. Yasuhara, LD-pumped 2.8 μm Er:Lu_2O_3 ceramic laser with 6.7 W output power and > 30% slope efficiency, Appl. Phys. Express. 14 (2020) 012001-1-4.
28. A.P. Safronov, O.M. Samatov, A.I. Medvedev, I.V. Beketov, A.M. Murzakaev, Synthesis of strontium hexaferrite nanopowder by the laser evaporation method, Nanotechnologies Russ. 7 (2012) 486-491.
29. L. Basyrova, R. Maksimov, V. Shitov, M. Baranov, V. Mikhaylovsky, A. Khubetsov, O. Dymshits, X. Mateos, P. Loiko, Effect of SiO_2 addition on structural and optical properties of Yb:$Lu_3Al_5O_{12}$ transparent ceramics based on laser ablated nanopowders, J. Alloys Compd. 806 (2019) 717–725.
30. S.N. Bagayev, V.V. Osipov, S.M. Vatnik, V.A. Shitov, I.A. Vedin, V.V. Platonov, I.Sh. Steinberg, R.N. Maksimov, Ho:YAG transparent ceramics based on nanopowders produced by laser ablation method: Fabrication, optical properties, and laser performance, Opt. Mater. 50 Part A (2015) 47-51.
31. N. D. Todorov, M. V. Abrashev, V. Marinova, M. Kadiyski, L. Dimowa, E. Faulques, Raman spectroscopy and lattice dynamical calculations of Sc_2O_3 single crystals, Phys. Rev. B 87 (2013) 104301.
32. J.C. Panitz, J.C. Mayor, B. Grob, W. Durisch, A Raman spectroscopic study of rare earth mixed oxides, J. Alloys Compd. 303 (2000) 340-344.

33. A.A. KaminskiЇ, K. Ueda, A.F. Konstantinova, H. Yagi, T. Yanagitani, A.V. Butashin, V.P. Orekhova, J. Lu, K. Takaichi, T. Uematsu, M. Musha, and A. Shirokava, Lasing and refractive indices of nanocrystalline ceramics of cubic yttrium oxide Y_2O_3 doped with Nd^{3+} and Yb^{3+} ions, Crystallogr. Rep. 48 (2003) 1041–1043.
34. K. Takaichi, H. Yagi, P. Becker, A. Shirakawa, K. Ueda, L. Bohatý, T. Yanagitani, A.A. Kaminskii, New data on investigation of novel laser ceramic on the base of cubic scandium sesquioxide: two-band tunable CW generation of Yb^{3+}:Sc_2O_3 with laser-diode pumping and the dispersion of refractive index in the visible and near-IR of undoped Sc_2O_3, Laser Phys. Lett. 4 (2007) 507–510.
35. H.R. Hoekstra, Phase relationships in rare earth sesquioxides at high pressure, Inorg. Chem. 5 (1966) 754–757.
36. A.E. Solovyova, Changes in the crystal structure and electrophysical properties of polycrystalline yttrium oxide upon heating in vacuum, Usp. Prikl. Fiz. 7 (2019) 177–187.
37. H. Yoshida, M. Kodo, K. Soga, T. Yamamoto, Doping effect on sinterability of polycrystalline yttria: From the viewpoint of cation diffusivity, J. Eur. Ceram. Soc. 32 (2012) 3103–3114.
38. S.J. Schneider, R.S. Roth, J.L. Waring, Solid state reactions involving oxides of trivalent cations, J. Res. Natl. Bur. Stand. 65A (1961) 345–374.
39. J.B. Clark, P.W. Richter, L.Du Toit, High-pressure synthesis of $YScO_3$, $HoScO_3$, $ErScO_3$, and $TmScO_3$, and a reevaluation of the lattice constants of the rare earth scandates, J. Solid State Chem. 23 (1978) 129–134.
40. E.S. Lukin, Modern high-density oxide-based ceramics with a controlled microstructure. Part V. Chemical-resistant high-density yttria-, scandia-, and alumina-based ceramics, Refract. Ind. Ceram. 38 (1997) 87–95.
41. Y. Shimizu, K. Ueda, Phase formation and UV luminescence of Gd^{3+} doped perovskite-type $YScO_3$, J. Solid State Chem. 242 Part 1 (2016) 170–174.
42. R.L. Coble, R.M. Cannon, in *Processing of Crystalline Ceramics* (ed. Palmour, H. III), pp. 151–168 (Materials Science Research, Vol. 11, Plenum, New York, 1978).
43. J.H. Mun, A. Jouini, A. Novoselov, A. Yoshikawa, T. Kasamoto, H. Ohta, H. Shibata, M. Isshiki, Y. Waseda, G. Boulon and T. Fukuda, Thermal and optical properties of Yb^{3+}-doped Y_2O_3 single crystal grown by the micro-pulling-down method, Jpn. J. Appl. Phys. 45 (2006) 5885–5888.
44. H. Hou, S. Zhou, T. Jia, H. Lin, H. Teng, Structural, thermal and mechanical properties of transparent Yb:$(Y_{0.97}Zr_{0.03})_2O_3$ ceramic, J. Eur. Ceram. Soc. 31 (2011) 733–738.